Faraday Discussions, DOI: 10.1039/d4fd00184b

The many faces of membrane tension for biomembranes and vesicles - ESI

Reinhard Lipowsky *

Max Planck Institute of Colloids and Interfaces,
14424 Potsdam, Germany

Electronic Supplementary Information (ESI) with the following sections, figures, and tables:

*Email: lipowsky@mpikg.mpg.de; URL: https://www.mpikg.mpg.de/rl/

S1 Short reminder about the theory of curvature elasticity

In the framework of curvature elasticity, we use a coarse-grained description of the membrane in terms of a smoothly curved surface, to which we can apply the concepts of differential geometry. Thus, the geometry of the membrane is described in terms of its principal curvatures, C_1 and C_2, which define the mean curvature M and the Gaussian curvature G *via*

$$M \equiv \tfrac{1}{2}\,(C_1 + C_2) \quad \text{and} \quad G \equiv C_1\, C_2\,. \tag{S1}$$

Curvature energy. Furthermore, the fluid membrane is now viewed as a thin elastic sheet, the behavior of which can be described by a few curvature-elastic parameters. We will focus here on the spontaneous curvature model[1–4] which has been shown to apply to GUV membranes with one or several phospholipids and cholesterol[5,6].

In the spontaneous curvature model, the curvature-elastic energy is equal to

$$E_{\rm cu} = E_{\rm be} + \int {\rm d}A\, \kappa_G\, G \tag{S2}$$

and the bending energy has the form

$$E_{\rm be} = 2\,\kappa \int {\rm d}A\, (M-m)^2\,. \tag{S3}$$

Both $E_{\rm cu}$ and $E_{\rm be}$ are given by integrals over the membrane area A and involve both the (local) mean curvature M and the (local) Gaussian curvature G of the membrane. Inspection of Eqs (S2) and (S3) shows that the curvature-elastic energy $E_{\rm cu}$ depends only on three curvature-elastic parameters: the bending rigidity κ, the spontaneous curvature m, and the Gaussian curvature modulus κ_G.

Furthermore, for the closed membrane surface of a vesicle, the area integral over the Gaussian curvature G depends only on the membrane topology, which can be characterized by the Euler characteristic χ or, equivalently, by the topological genus $\mathfrak{g} = 1 - \frac{1}{2}\,\chi$. As a consequence, the Gaussian curvature energy is equal to

$$E_G \equiv \int {\rm d}A\, \kappa_G\, G = 2\pi\chi\,\kappa_G = 2\pi(2-2\mathfrak{g})\,\kappa_G \tag{S4}$$

as follows from the Gauss-Bonnet theorem of differential geometry[7]. Thus, in the absence of topological transformations, the Gaussian curvature energy contributes a topological constant that does not affect the vesicle shape. As a consequence, we are then left with two curvature-elastic parameters, the bending rigidity κ and the spontaneous curvature m.

Shape functional for vesicle shapes In order to determine the shapes of giant vesicles, one has to impose additional constraints on the vesicle volume V and membrane area A. These constraints are taken into account via two Lagrange multiplier, ΔP and Σ', which are conjugate to volume V and area A. The vesicle shape is then obtained by minimization of the elastic shape functional

$$F_{\rm el} = -\Delta P\, V + \Sigma' A + E_{\rm be} \tag{S5}$$

for fixed volume V and fixed area A. Both Lagrange multipliers have a simple physical interpretation. The Lagrange multiplier ΔP is equal to the pressure difference

$$\Delta P = P_{\rm in} - P_{\rm ex} \tag{S6}$$

between the interior pressure $P_{\rm in}$ within the vesicle compartment and the exterior pressure $P_{\rm ex}$ in the external compartment. Furthermore, it turns out that the Langrange multiplier Σ' is equal to the mechanical membrane tension Σ, that is,[8]

$$\Sigma' = \Sigma = K_A(A - A_0)/A_0 \tag{S7}$$

where we used the expression for the mechanical tension Σ in Eq (1) of the main text. This identity holds for all stable vesicle shapes as described by local minima of the shape functional $F_{\rm el}$ and for all saddle points of $F_{\rm el}$.

Shape parameters and morphology diagram. The shape functional $F_{\rm el}$ in Eq (S5) depends (i) on two curvature-elastic parameters, the bending rigidity κ and the spontaneous curvature m, which determine the elastic bending energy $E_{\rm be}$ in Eq (S3), as well as (ii) on two geometric parameters, the vesicle volume V and the membrane area A. Using the vesicle size $R_{\rm ve}$ as defined by

$$R_{\rm ve} \equiv \sqrt{A/(4\pi)} \tag{S8}$$

as the unit of length and the bending rigidity κ as the unit of energy, we obtain two dimensionless shape parameters as given by the volume-to-area ratio

$$\bar{v} \equiv \frac{V}{\frac{4\pi}{3}R_{\rm ve}^3} = 6\sqrt{\pi}\frac{V}{A^{3/2}} \tag{S9}$$

and by the rescaled spontaneous curvature

$$\bar{m} \equiv mR_{\rm ve}\,. \tag{S10}$$

The volume-to-area ratio $\bar{v}$ is limited to the range $0 < \bar{v} \leq 1$ where the upper limit $\bar{v} = 1$ corresponds to a spherical shape as follows from the isoperimetric inequality.[9,10] Any vesicle shape can now be specified in terms of the two shape parameters $\bar{v}$ and $\bar{m}$, which define the morphology diagram.

Measurement of curvature-elastic tension. Micropipette aspiration of tubulated vesicles as in Fig S1 a can be used to measure the curvature-elastic tension $\sigma = 2\kappa m^2$ defined in Eq (5). Experimental data for giant vesicles enclosed by POPC membranes and doped with the glycolipid (or ganglioside) GM1 are shown in Fig S1 b. These micropipette experiments are challenging because they require very low aspiration pressures.

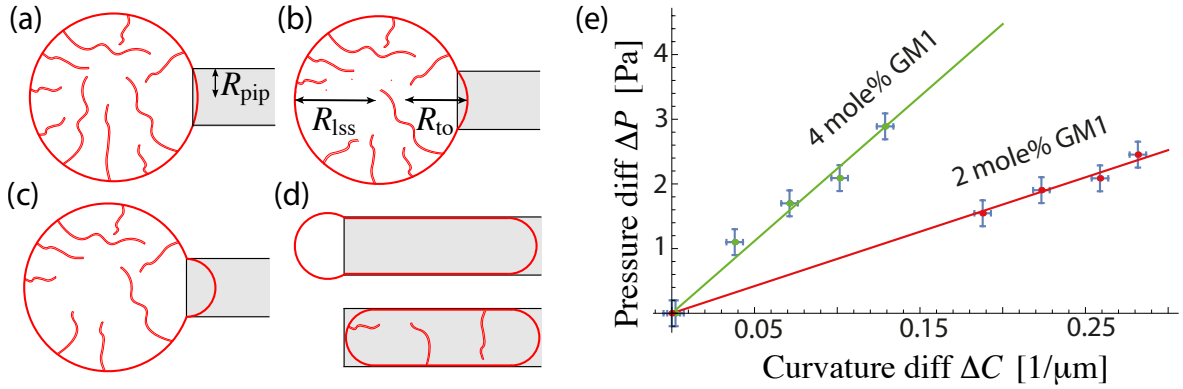

Figure S1 (a-d) Tube retraction from a tubulated GUV (red) by micropipette aspiration: (a) The spherical vesicle comes into contact with a micropipette of radius $R_{\rm pip}$; (b) With increasing suction pressure, some of the nanotubes are retracted, the vesicle develops a tongue that has the form of a spherical cap with radius $R_{\rm to}$, and the large spherical membrane segment outside of the pipette attains the radius $R_{\rm lss}$; (c) When the suction pressure reaches a critical value, the cap-like tongue becomes a hemisphere with radius $R_{\rm to} = R_{\rm pip}$, and the vesicle membrane starts to flow into the micropipette; (d) Depending on the membrane area stored in the nanotubes, the flow within the membrane stops as soon as all nanotubes have been retracted (d, top) or continues until the vesicle is completely aspirated into the pipette (d, bottom); and (e) Direct measurement of the curvature-elastic tension $\sigma = 2\kappa m^2$: Aspiration pressure ΔP versus curvature difference $\Delta C = 2/R_{\rm to} - 2/R_{\rm lss}$ for 2 and 4 mole % GM1. The data are well fitted by the linear relation $\Delta P \approx \sigma \Delta C$, leading to $\sigma = (8.33 \pm 0.76)$ Pa μm and $\sigma = (22.2 \pm 1.5)$ Pa μm for 2 and 4 mole % GM1, respectively.[11]

S2 Shape fluctuations of interfaces and membranes

Liquid-liquid interfaces and fluid membranes are two-dimensional surfaces embedded in three spatial dimensions. The scaling properties of these fluctuations can be understood from simple scaling arguments, which distinguish between "humps" of rough and "blobs" of crumpled surfaces as in Fig S2 . From a conceptual point of view, it is useful to generalize the surface geometry and to consider $(d-1)$-dimensional "surfaces" in d-dimensions. For $d=2$, we then have one-dimensional domain boundaries governed by line tension (Fig S2 a) or flexible chain molecules of intrinsic length $L_{\rm in}$ (Fig S2 b).]]

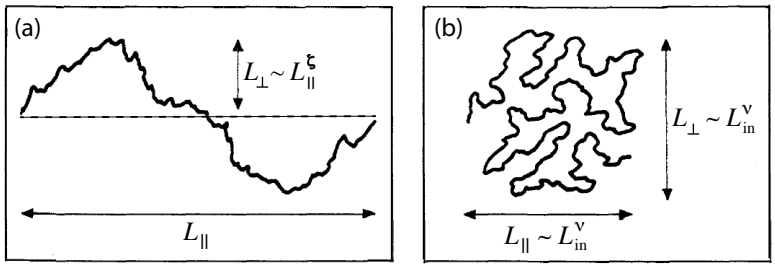

Figure S2 (a) One-dimensional domain boundary, which is, on average, parallel to the horizontal dashed line. A boundary segment of projected length $L_\parallel$ forms an anisotropic "hump" of perpendicular extension $L_\perp \sim L_\parallel^\zeta$ with roughness exponent $\zeta = 1/2$; and (b) Flexible chain molecule of intrinsic length $L_{\rm in}$ forms an isotropic "blob" of linear extension $L_\parallel \sim L_\perp \sim L_{\rm in}^\nu$ with the Flory exponent $\nu = 3/4$ in two dimensions.

Statistical weight of shape fluctuations. Now, consider a two-dimensional surface with projected area $A_\parallel = L_\parallel^2$. In the absence of shape fluctuations, such a surface attains a planar or flat state. The shape fluctuations of this surface are parametrized by $z = h(x_1,x_2) = h(\vec{x})$ with the height variable h, which represents the local displacements of the surface from its flat state with $h(\vec{x}) = 0$. This Monge parametrization implicitly assumes that the surface does not fold back on itself and that such overhangs of the surface can be ignored. This assumption is fulfilled as long as the gradients of h, corresponding to $\partial h/\partial x_1$ and $\partial h/\partial x_1$, are small.

For small gradients of h, the excess surface area arising from the shape fluctuations of the planar surface leads to the excess energy

$$\Delta E\{h\} = \int {\rm d}A_\parallel \left[\tfrac{1}{2}\,\Sigma' \left(\nabla h\right)^2 + \tfrac{1}{2}\,\kappa' \left(\nabla^2 h\right)^2\right] \tag{S11}$$

which depends on the tension parameter Σ' and the rigidity parameter κ'. For a fluid membrane with $\Sigma' = \Sigma$ and $\kappa' = \kappa$, this excess energy corresponds to the small gradient approximation of the shape functional in Eq (S5) with zero pressure difference, $\Delta P = 0$, and zero spontaneous curvature, $m = 0$. For a liquid-liquid interface, the tension parameter Σ' is equal to the interfacial tension $\Sigma_{\rm int}$, which is positive as required by the thermodynamic stability of the planar interface. Furthermore, we take $\kappa' = 0$ for a liquid-liquid interface.

Scaling properties of shape fluctuations. Using the Boltzmann factor $\propto \exp[-\Delta E\{h\}/(k_{\rm B}T)]$ with $\Delta E\{h\}$ as in Eq (S11), the perpendicular excursions of the surface humps can be estimated from the expectation value $\langle (h - \langle h\rangle)^2\rangle = \langle h^2\rangle$. A Fourier decomposition of the displacement field $h(\vec{x})$ then leads to

$$\langle (h - \langle h\rangle)^2\rangle = \langle h^2(\vec{x})\rangle = \int \frac{{\rm d}^2 q}{(2\pi)^2}\,\frac{k_{\rm B}T}{\Sigma' q^2 + \kappa' q^4} = \int \frac{dq}{2\pi}\, q\,\frac{k_{\rm B}T}{\Sigma' q^2 + \kappa' q^4} \tag{S12}$$

The q-integral involves two cutoffs, $q_{\rm max} \propto 1/\ell$ and $q_{\rm min} \propto 1/L_\parallel$, with the molecular length scale ℓ and the linear extension $L_\parallel$ of the projected surface area. For a liquid-liquid interface with $\Sigma' = \Sigma_{\rm int}$ and $\kappa' = 0$, one obtains [12]

$$\langle (h - \langle h\rangle)^2\rangle = \int \frac{dq}{2\pi}\,\frac{k_{\rm B}T}{\Sigma'_{\rm int} q} \approx \frac{k_{\rm B}T}{\Sigma_{\rm int}}\,\frac{1}{2\pi}\ln(L_\parallel/\ell) \tag{S13}$$

where the asymptotic equality holds in the limit of large $L_\parallel$. This relationship implies interface humps with $L_\perp^2 \sim \ln(L_\parallel/\ell)$. On the other hand, for a tensionless membrane with $\Sigma' = 0$ and $\kappa' = \kappa$, the expression in Eq (S12) becomes [13]

$$\langle (h - \langle h\rangle)^2\rangle = \int \frac{dq}{2\pi}\,\frac{k_{\rm B}T}{\kappa q^3} \approx \frac{k_{\rm B}T}{4\pi\kappa}\,\frac{1}{q_{\rm min}^2} \sim \frac{k_{\rm B}T}{\kappa} L_\parallel^2\,, \tag{S14}$$

which implies membrane humps with $L_\perp^2 \sim L_\parallel^2$.

The overall gradient of the surface humps scales as $(L_\perp/L_\parallel)$.[14] Thus, the overall gradient of a two-dimensional interface with $L_\perp \sim \sqrt{\ln(L_\parallel/\ell)}$ decreases as $\sqrt{\ln(L_\parallel/\ell)}/L_\parallel$ for large $L_\parallel$. On the other hand, the overall gradient of a two-dimensional fluid membrane with $L_\perp \sim L_\parallel$ behaves as $L_\perp/L_\parallel \sim L_\parallel^0$ which does *not* decrease for large $L_\parallel$. Additional insight into the large-scale behavior of membrane humps can be obtained from the correlation function for the normal vectors as determined in the next paragraph.

Correlation function of membrane's normal vectors. The normal vector $\hat{n}$ to the membrane surface at point $[\vec{x}, h(\vec{x})]$ has the form

$$\hat{n}(\vec{x}) = (-h_1, -h_2, 1)/\sqrt{1+h_1^2+h_2^2} \quad \text{with} \quad h_i \equiv \frac{\partial h}{\partial x_i}\Big|_{\vec{x}}. \tag{S15}$$

For small h_i, the three-dimensional normal vector $\hat{n}$ reduces to

$$\hat{n}(\vec{x}) \approx (-h_1, -h_2, 1) \tag{S16}$$

and the normal-normal correlation function $C_n \equiv \frac{1}{2}\langle [\hat{n}(\vec{x}) - \hat{n}(\vec{0})]^2 \rangle$ attains the form

$$C_n(x) \approx \tfrac{1}{2}\langle [\nabla h(\vec{x}) - \nabla h(\vec{0})]^2 \rangle = \langle [\nabla h(\vec{0})]^2 - \nabla h(\vec{x}) \nabla h(\vec{0})] \rangle . \tag{S17}$$

For a tensionless membrane, the Fourier decomposition of the displacement field h then leads to

$$C_n(x) \approx k_{\rm B}T \int \frac{{\rm d}^2 q}{(2\pi)^2} \frac{1 - e^{i\vec{q}\cdot\vec{x}}}{\kappa q^2} = \frac{k_{\rm B}T}{2\pi\kappa} \int {\rm d}q \, \frac{1 - J_0(qx)}{q} \tag{S18}$$

where $J_0(y)$ is a Bessel function[15] with $y = qx = |\vec{q}\,|\,|\vec{x}|$. The correlation function C_n as given by Eq (S18) was studied by De Gennes and Taupin[16] in the context of tensionless interfaces in microemulsions and led to their proposal of a finite persistence length for such interfaces.

For tensionless membranes as considered here, a finite persistence length was observed in Monte Carlo simulations of dynamically triangulated surfaces.[17] Above the persistence length, the membranes attain crumpled states as displayed in Fig S3 for two different values of the rescaled bending rigidity $\kappa/(k_{\rm B}T)$. The scaling behavior of these crumpled states has been analyzed in analogy to the scaling behavior of branched polymers.

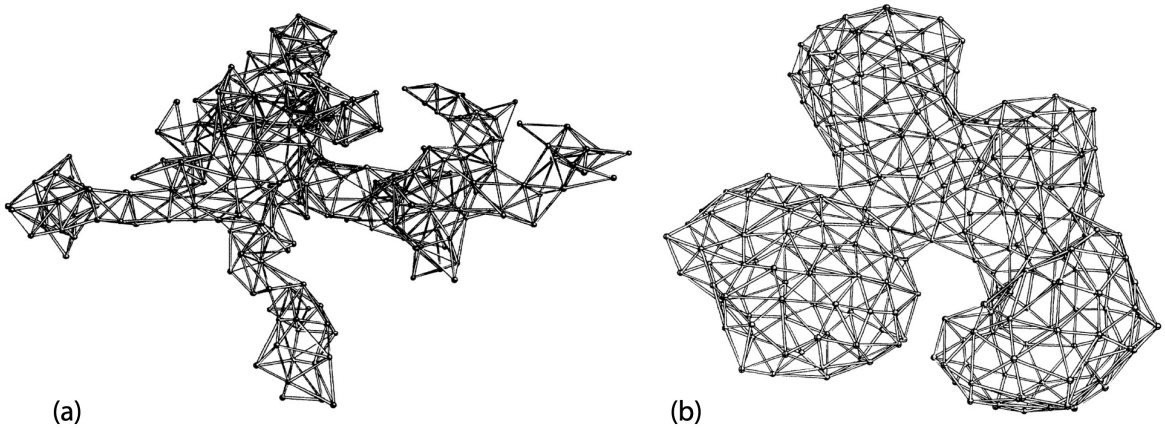

Figure S3 Crumpled states of vesicle membranes in their fluid state with linear dimensions that exceed the peristence length ξ_p in Eq (6). The membranes are discretized as dynamically triangulated surfaces with rescaled bending rigidity $\kappa/(k_{\rm B}T) = 0.35$ in (a) and $\kappa/(k_{\rm B}T) = 2.4$ in (b). Both configurations in (a) and (b) belong to the parameter regime, in which the scaling behavior of the vesicle membranes is analogous to the behavior of branched polymers. It is interesting to note that the membrane configuration in (b) resembles a multispherical vesicle with open necks. Reused with permission from ref. 17, Americal Physical Society, 1995.

S3 Bilayer and leaflet tensions of planar bilayers

For a planar bilayer, the stress profile, denoted by $s = s(z)$, depends on the coordinate z perpendicular to the bilayer. The mechanical tension Σ of the planar bilayer is then obtained by

$$\Sigma = \int_{-\infty}^{+\infty} \mathrm{d}z\, s(z)\,, \tag{S19}$$

that is, by integrating the whole stress profile $s(z)$ over z. In practise, the stress profile $s(z)$ decays rather fast away from the bilayer, which implies that one can restrict the integration by some cut-off values $z_{\min}$ and $z_{\max}$.

In order to decompose the bilayer tension Σ into the two leaflet tensions, we now distinguish the lower from the upper leaflet by the subscripts ll and ul and denote the corresponding leaflet tensions by Σ_{ll} and Σ_{ul}. The lower leaflet occupies a certain range of z-values, which lie below the z-values for the upper leaflet. The molecular interface between these two leaflets defines the midplane of the planar bilayer at $z = z_{\mathrm{mid}}$.[18–20] The leaflet tensions are then obtained from

$$\Sigma_{ll} = \int_{-\infty}^{z_{\mathrm{mid}}} \mathrm{d}z\, s(z) \quad \text{and} \quad \Sigma_{ul} = \int_{z_{\mathrm{mid}}}^{+\infty} \mathrm{d}z\, s(z) \tag{S20}$$

which imply the bilayer tension $\Sigma = \Sigma_{ll} + \Sigma_{ul}$. Each leaflet tension can be negative, zero, or positive and then leads to a compressed, tensionless, or stretched leaflet as schematically shown in Fig S4 .

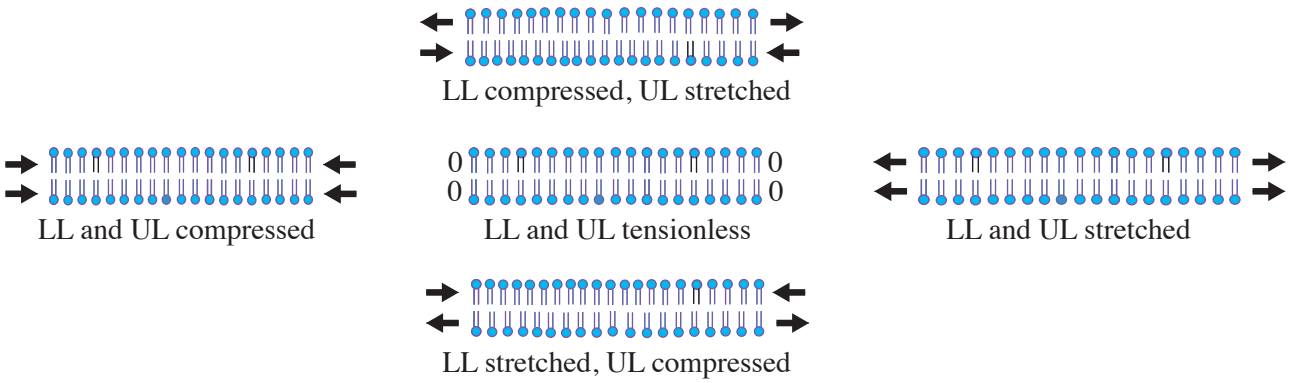

Figure S4 Both the lower leaflet (LL) and the upper leaflet (UL) of a planar lipid bilayer can be compressed, tensionless, or stretched, when its leaflet tension is negative, zero, or positive. As indicated by the arrows, a compressed leaflet is subject to a negative leaflet tension whereas a stretched leaflet experiences a positive leaflet tension. For the elastic state in the middle, both leaflets experience zero leaflet tensions and are, thus, tensionless, which defines the reference state of the bilayer with optimal area per lipid and optimal volume per lipid. The distinction between compressed, tensionless, and stretched leaflets also applies to vesicle bilayers. It is important to note that, in contrast to a lipid bilayer, a soap film is enclosed by two liquid-gas interfaces, both of which have a positive interfacial tension. Thus, if one wants to draw an analogy between a lipid bilayer and a soap film, this analogy is restricted to the elastic state on the right, for which both leaflets are stretched.

S4 Elastic deformations of symmetric bilayers

First, let us consider a planar and symmetric bilayer consisting of N lipids, with $N/2$ lipids assembled in each leaflet. For simplicity, we will focus on a one-component bilayer. If the bilayer contains several lipid components, the bilayer is symmetric if both leaflets have the same uniform composition. A planar and symmetric bilayer is subject to equal leaflet tensions, $\Sigma_{ul} = \Sigma_{ll}$, corresponding to the red data points in Fig 3 of the main text. By increasing the projected area $A_{\parallel}$ which is the base area of the simulation box, we also increase the relative area dilation

$$\Delta a \equiv (A_{\parallel} - A_0)/A_0 = (a - a_0)/a_0 \tag{S21}$$

where we introduced the area per lipid, $a \equiv 2A_{\parallel}/N$, and the optimal area per lipid, a_0. The relative area dilation Δa of a symmetric bilayer determines the mechanical tension Σ via $\Sigma = K_A \Delta a$ as in Eq (1) of the main text.

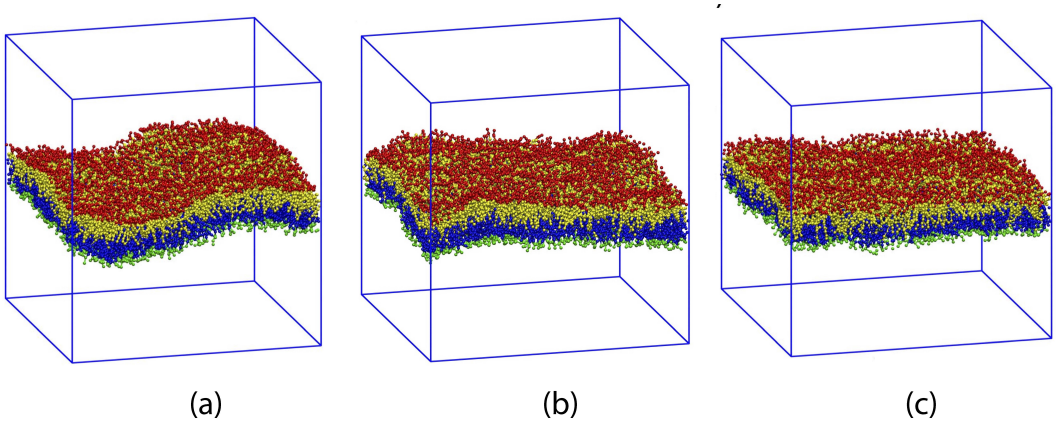

Figure S5 Elastic ELT deformations of a symmetric planar bilayer with 841 lipids in each leaflet: Simulation snapshots of such a bilayer for three different base areas of the simulation box corresponding to (a) a compressed, (b) the tensionless, and (c) a stretched bilayer. respectively.[21] The volume of the simulation box has the same value in all three cases. The resulting leaflet tension $\Sigma_{\rm le} = \Sigma_{ll} = \Sigma_{ul}$ is displayed in Fig S6 as a function of area per lipid and volume per lipid.

It is useful to introduce the area compressibilities of the individual leaflets via

$$\Sigma_{ll} = K_{ll} \frac{a_{ll} - a_0}{a_0} \quad \text{and} \quad \Sigma_{ul} = K_{ul} \frac{a_{ul} - a_0}{a_0} \tag{S22}$$

where we took into account that the tensionless lower and the tensionless upper leaflet have the same area per lipid, a_0. A symmetric bilayer is also characterized by $a_{ll} = a_{ul}$ and $K_{ll} = K_{ul}$. The bilayer tension $\Sigma = \Sigma_{ll} + \Sigma_{ul}$ of a planar and symmetric bilayer is then governed by the area compressibility $K_A = K_{ll} + K_{ul} = 2K_{ll} = 2K_{ul}$.

Alternatively, we may describe the elastic response of the planar bilayer in terms of volume per lipid, v, as determined by Voronoi tesselation and introduce the lateral volume compressibilities B_{ll} and B_{ul} of the two leaflets by[21]

$$\Sigma_{ll} = B_{ll} \frac{v_{ll} - v_0}{v_0} \quad \text{and} \quad \Sigma_{ul} = B_{ul} \frac{v_{ul} - v_0}{v_0}, \tag{S23}$$

where the tensionless lower and the tensionless upper leaflet have the same volume per lipid, v_0. A symmetric bilayer is also characterized by $v_{ll} = v_{ul}$ and $B_{ll} = B_{ul}$. It then follows from $\Sigma = \Sigma_{ll} + \Sigma_{ul}$ that the lateral volume compressibility $B_{\rm sy}$ of a planar and symmetric bilayer satisfies $B_{\rm sy} = B_{ll} + B_{ul} = 2B_{ll} = 2B_{ul}$.

For the geometry of planar bilayers, both the area per lipid, a, and the volume per lipid, v, can be defined in a unique manner. This equivalence no longer applies for vesicle bilayers. Indeed, in order to define an area per lipid for vesicle bilayers, one necessarily has to project the curved leaflets onto some auxiliary surfaces. The deduced area per lipid depends on the ambiguous choice of these auxiliary surfaces. In contrast, the volume per lipid is uniquely defined by means of Voronoi tessellation, as illustrated in Fig S7 for planar bilayers.

One should note that the simple relationships $K_A = K_{ll} + K_{ul}$ and $B_{\rm sy} = B_{ll} + B_{ul}$ between the bilayer compressibilities and the leaflet compressibilities do not hold for planar and *asymmetric* bilayers with $a_{ll} \neq a_{ul}$ and $v_{ll} \neq v_{ul}$. Likewise, these relationships do not apply to vesicle bilayers, see Sect 4 of the main text.

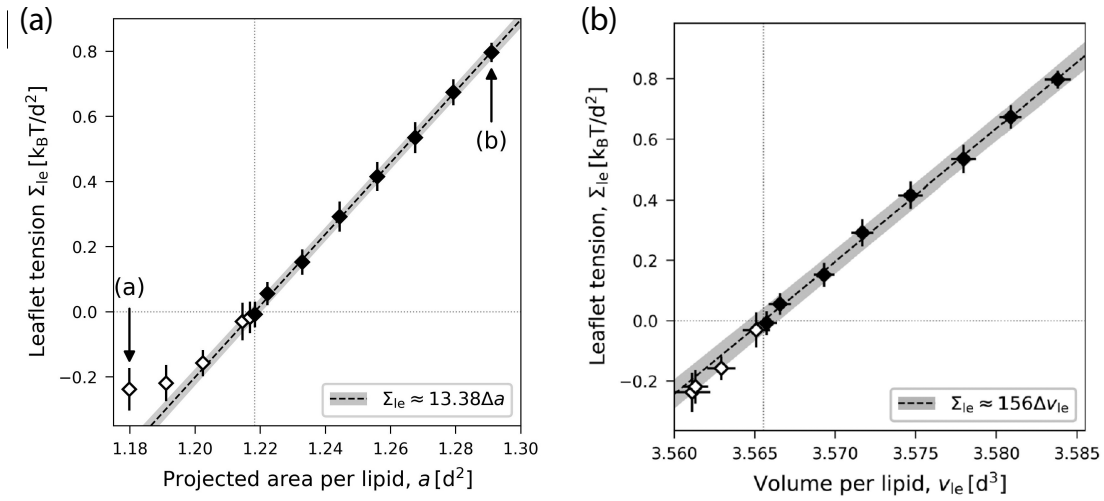

Figure S6 Leaflet tension $\Sigma_{le} = \Sigma_{ll} = \Sigma_{ul}$ of a planar and symmetric planar bilayer versus projected area per lipid in (a) and versus volume per lipid in (b).[21] The volumes per lipid were determined by Voronoi tesselation as in Fig S7 . Slope and intercept of the linear fit define the values of the area compressibility and the lateral volume compressibility as follows from Eqs (S22) and (S23).

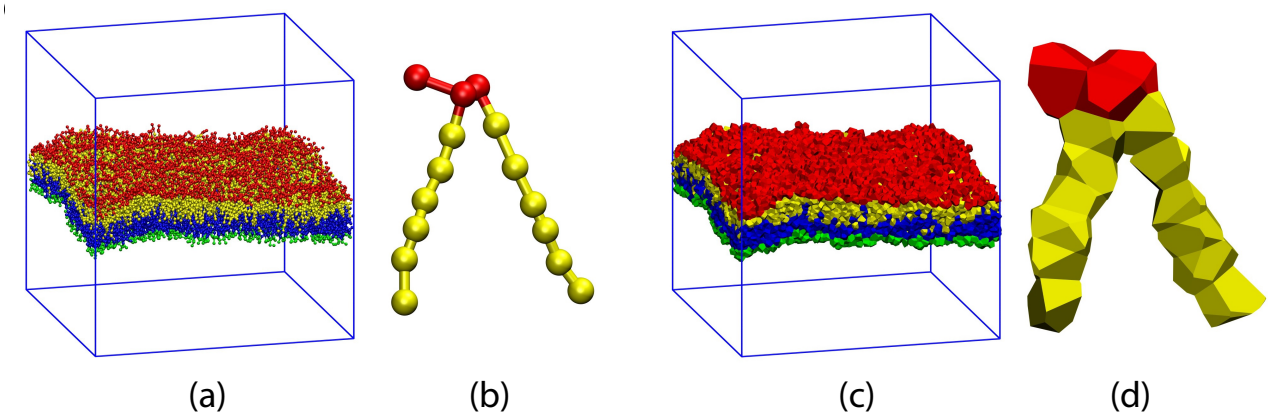

Figure S7 Three-dimensional Voronoi tessellation of the molecular model built up from different types of beads: (a) Conformation of a planar and symmetric bilayer with $N_{ll} = N_{ul} = 841$ and tensionless leaflets. The lipids in the lower leaflet have green head groups and blue chain beads; the lipids in the upper leaflet have red head groups and yellow chain beads; (b) Typical conformation of a single lipid molecule within the upper leaflet in ball-and-stick representation; (c) Voronoi cells assigned to each bead of the bilayer in panel a; and (d) Voronoi cells assigned to each bead of the lipid molecule in panel b.[21]

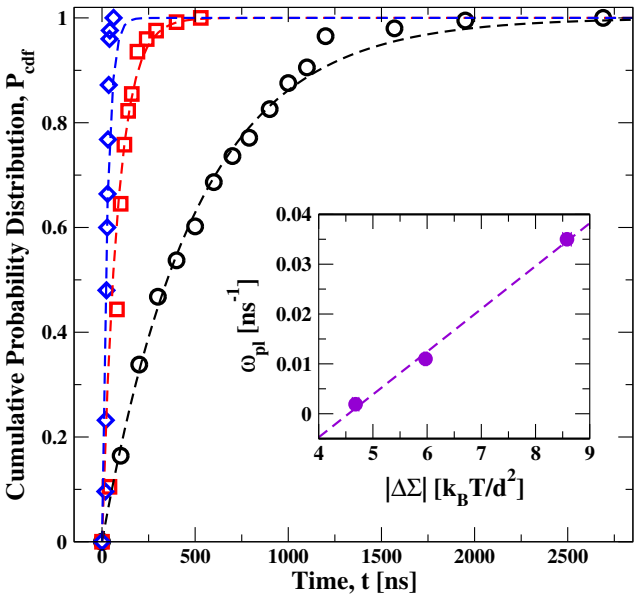

Figure S8 Cumulative distribution function $P_{\rm cdf}$ versus time t, for planar and tensionless bilayers with N_{ul} lipids in the upper leaflet and $N_{ll} = 1682 - N_{ul}$ lipids in the lower leaflet.[22] Three sets of data for $N_{ul} = 986$ (black circles), $N_{ul} = 1015$ (red squares), and $N_{ul} = 1073$ (blue diamonds). These data sets are well fitted, using least squares, by an exponential distribution (broken lines) Inset: Monotonic increase of the flip-flop rate $\omega_{\rm pl}$ with the absolute value $|\Delta\Sigma| = |\Sigma_{ul} - \Sigma_{ll}|$ of the stress asymmetry.

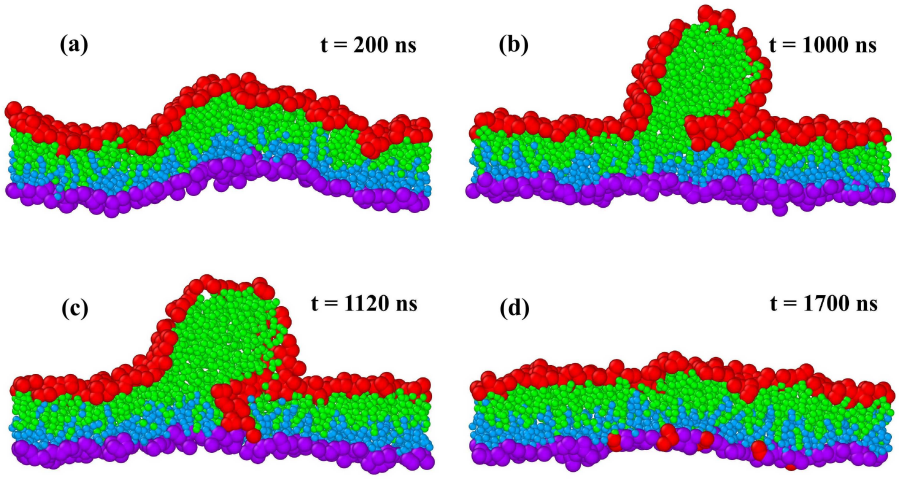

Figure S9 Structural instability and self-healing of a tensionless and asymmetric planar bilayer.[22] At time $t = 0$, the bilayer is initially assembled from $N_{ul} = 986$ red-green lipids in the compressed upper leaflet and from $N_{ll} = 696$ purple-blue lipids in the stretched lower leaflet: (a) At $t = 200$ ns, the metastable bilayer bulges towards the upper leaflet; (b) At $t = 1000$ ns, a globular micelle has been formed from about 100 red-green lipids that were expelled from the upper leaflet; (c) At $t = 1120$ ns, red-green lipids move towards the stretched lower leaflet along the contact line between micelle and bilayer; and (d) This lipid exchange leads to a self-healing process of the bilayer that is completed at $t = 1700$ ns. At this time point, 93 red-green lipids have moved from the upper to the lower leaflet. The restored bilayer remains stable without flip-flops until the end of the simulations at $t = 12.5\,\mu$s.

S5 Relaxation of leaflet tensions via frequent lipid flip-flops

Consider a tensionless planar bilayer with opposite leaflet tensions and several lipid components, including one component that undergoes frequent flip-flops. These flip-flops act to reduce the magnitude of the leaflet tensions and to move the bilayer towards the relaxed reference state with tensionless leaflets. Such a relaxation process has been observed in molecular dynamics simulations of a lipid bilayer that contained the phospholipid POPC and the glycolipid (ganglioside) GM1, both of which do not undergo flip-flops, and, in addition, a model cholesterol, which moved frequently from one leaflet to the other, as schematically shown in Fig. S10 .[23]

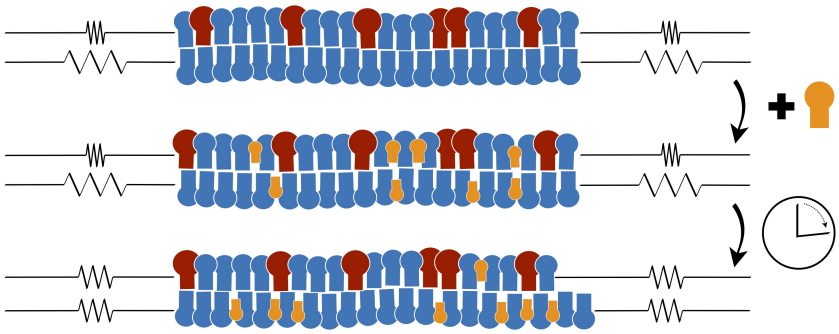

Figure S10 (Top) Bilayer membrane with two lipid components (blue and red) that do not undergo flip-flops from one leaflet to the other. The bilayer tension $\Sigma = \Sigma_{ll} + \Sigma_{ul}$ is (close to) zero, with a compressed upper leaflet and a stretched lower leaflet; (Middle) Cholesterol (orange) is added as a third component to both leaflets so that they initially contain the same number of cholesterol molecules; and (Bottom) After the cholesterol has been redistributed by flip-flops, both leaflets have attained a tensionless state as indicated by the relaxed springs.[23]

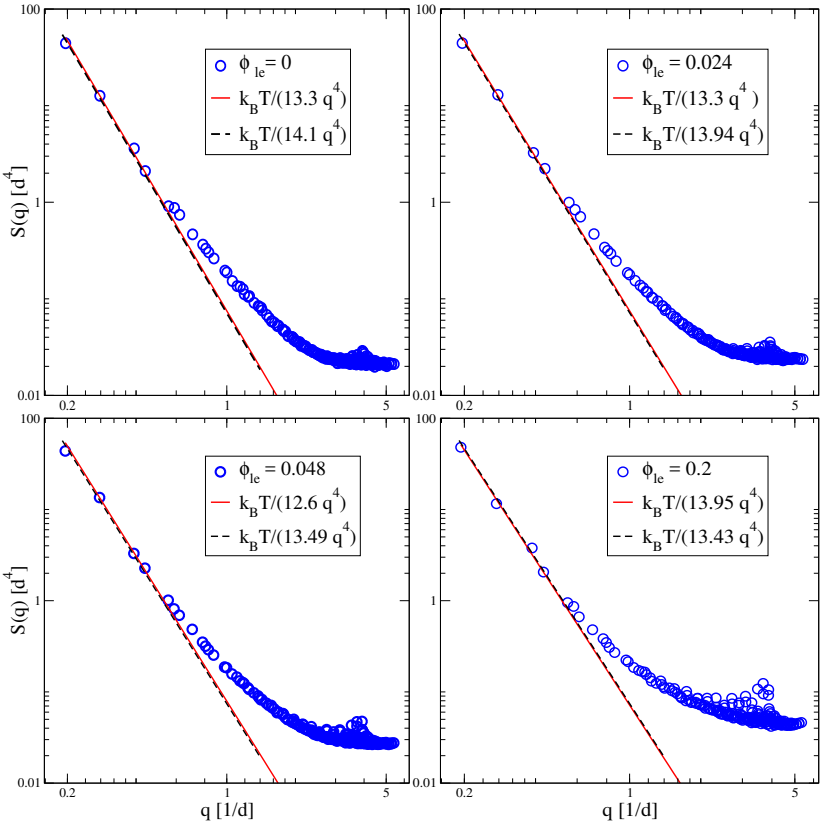

Figure S11 Fluctuation spectra $S(q)$ of symmetric and tensionless bilayers with two lipid components as a function of wavenumber q. The different panels belong to different lipid mole fractions $\phi_{\rm le}$ of one lipid component, which has the same value in both leaflets. For all mole fractions, the low-q part of the spectrum behaves as $S(q) \sim k_{\rm B}T/(\kappa q^4)$ with composition-dependent κ-values. These bending rigidities κ satisfy the relationship $\kappa = K_A \ell_{\rm me}^2/48$ for all lipid compositions with the area compressibility modulus K_A and the membrane thickness $\ell_{\rm me}$, as determined by independent analysis.[24]

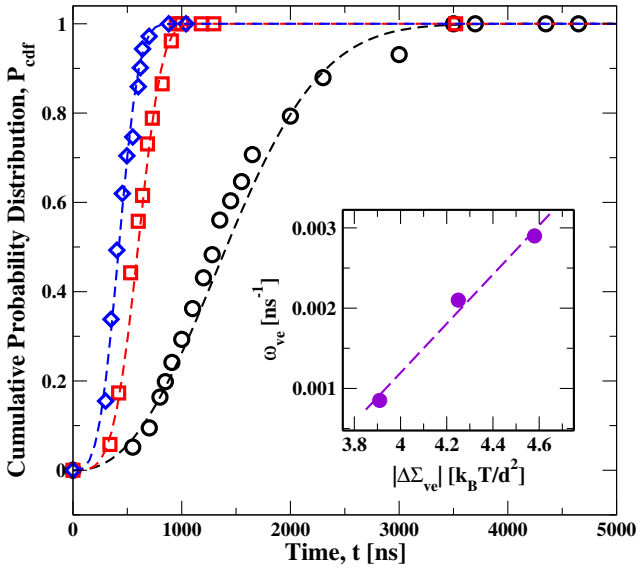

Figure S12 Cumulative distribution function $P_{\rm cdf}$ versus time t for tensionless vesicle bilayers with N_{ol} lipids in the outer and $N_{il} = 2875 - N_{ol}$ lipids in the inner leaflets. Three sets of data are displayed with $N_{ol} = 2105$ (black circles), $N_{ol} = 2125$ (red squares), and $N_{ol} = 2150$ (blue diamonds) lipids in the outer leaflet, which belong to the left instability regime in Fig 6 of the main text. Each cumulative distribution has a sigmoidal shape and can be fitted to a Weibull distribution with dimensionless shape parameter $k > 0$ and rate paramter $\omega_{\rm ve}$.[22] Inset: Monotonic increase of the rate parameter $\omega_{\rm ve}$ with the absolute value $|\Delta\Sigma_{\rm ve}|$ of the stress asymmetry.

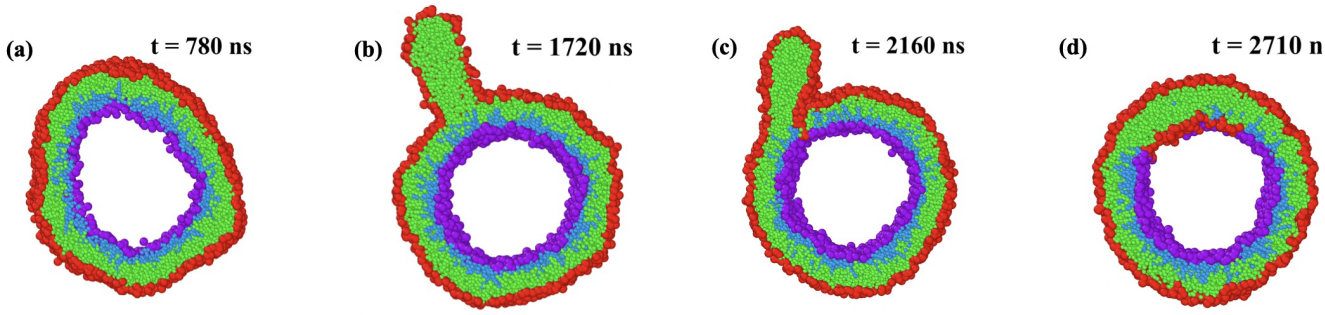

Figure S13 Stress-induced instability and self-healing of a vesicle bilayer that consists of $N_{ol} + N_{il} = 2875$ lipids in both leaflets.[22] At time $t = 0$, the bilayer is assembled from $N_{ol} = 2105$ and $N_{il} = 770$ lipids and the vesicle volume is adjusted in such a way that the outer leaflet is compressed by the negative leaflet tension $\Sigma_{ol} = -1.97\, k_{\rm B}T/d^2$ and the inner leaflet is stretched by the positive leaflet tension $\Sigma_{il} = +1.94\, k_{\rm B}T/d^2$: (a) At $t = 780$ ns, the compressed outer leaflet leads to some kinky bilayer deformations; (b) At $t = 1720$ ns, a cylindrical micelle has been formed from about 180 red-green lipids that were expelled from the outer leaflet; (c) At $t = 2160$ ns, lipids move towards the stretched inner leaflet along the contact line between micelle and bilayer; and (d) At $t = 2710$ ns, the self-healing process via stress-induced lipid exchange has been completed and 111 red-green lipids have moved to the inner leaflet. The restored bilayer undergoes no further flip-flops until the end of the simulations.

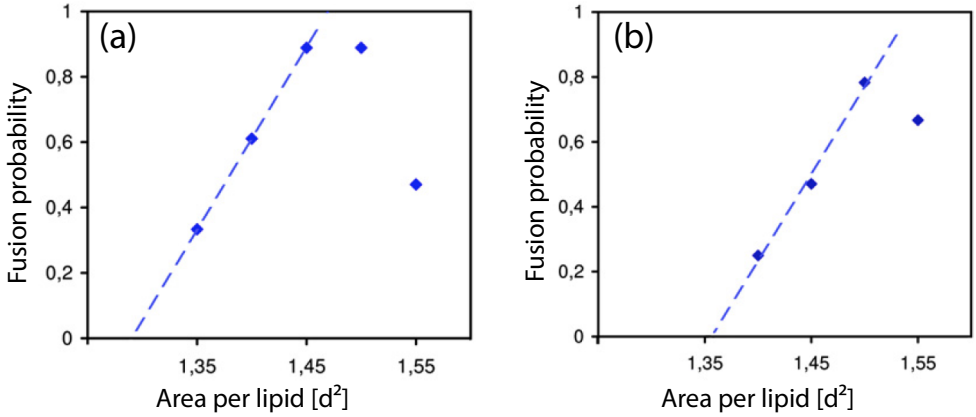

Figure S14 Fusion probability for nanovesicles interacting with planar bilayers versus rescaled area per lipid, $\bar{a} \equiv a/d^2$, for vesicles with a diameter of 14 nm in (a) and a diameter of 28 nm in (b). In both cases, the fusion probability, which represents the fraction of fusion attempts that lead to fusion within 20 μs, exhibits a maximum at $\bar{a}_{\max}$ with $1.45 < \bar{a}_{\max} < 1.5$ in (a) and $\bar{a}_{\max} \simeq 1.5$ in (b) corresponding to the bilayer tensions $\bar{\Sigma} \equiv \Sigma d^2/k_{\rm B}T \simeq 3.36$ and $\bar{\Sigma} \simeq 4.25$, respectively. At higher tensions, fusion becomes less likely because of membrane rupture; at lower tensions, fusion is more and more replaced by adhesion or hemifusion. A linear extrapolation of the data to smaller values of $\bar{a}$ indicates a fusion threshold for area per lipid and, thus, for bilayer tension, $\bar{\Sigma}_{\rm th}$. Reused with permission from ref. 25, Elsevier, 2009.

S6 General properties of multispherical vesicle shapes

Local shape equation for spherical membrane segments. The local shape equation is obtained by minimizing the elastic shape functional $F_{\rm el}$ in Eq (3) of the main text. In general, this local shape equation is quite difficult to solve but becomes much simpler for spherical membrane segments. Indeed, for a spherical segment with constant mean curvature $M = M_{\rm sp}$, this mean curvature satisfies the quadratic equation

$$\Delta P = 2\Sigma_{\rm tot} M_{\rm sp} - 4\kappa m M_{\rm sp}^2 \tag{S24}$$

with the total membrane tension

$$\Sigma_{\rm tot} \equiv \Sigma + 2\kappa m^2 \,. \tag{S25}$$

A detailed case-by-case analysis[26] shows that there are only two physically acceptable roots to the quadratic shape equation in Eq (S24). For positive spontaneous curvature, one obtains two positive roots for this equation with the mean curvature $M_{\rm sp} = M_l = 1/R_l > 0$ of large spheres with radius R_l and the mean curvature $M_{\rm sp} = M_s = 1/R_s > 0$ of small spheres with radius $R_s \leq R_l$. The degenerate case with $R_s = R_l = R_*$ corresponds to several equally sized spheres. For negative spontaneous curvature, one obtains one positive root and one negative root, corresponding to the positive mean curvature $M_{\rm sp} = M_l = 1/R_l > 0$ of one large spherea with radius R_l and the negative mean curvature $M_{\rm sp} = M_s = -1/R_s < 0$ for one or several small spheres of radius R_s.

Geometry of multispheres. The geometry of a multispherical shape, consisting of large and small spheres connected by closed membrane necks, depends only on one shape parameter, the volume-to-area ratio $\bar{v}$ but is independent of the second shape parameter as provided by the spontaneous curvature $\bar{m} = mR_{\rm ve}$. [lipo412] To derive this property, it is convenient to introduce the dimensionless sphere radii r_l and r_s via

$$r_l \equiv R_l/R_{\rm ve} \quad \text{and} \quad r_s \equiv R_s/R_{\rm ve} \tag{S26}$$

with the vesicle size $R_{\rm ve} = \sqrt{A/(4\pi)}$ as defined by Eq (S8).

Now, consider a membrane of area A, which forms a multisphere with N_l large and N_s small spheres. When expressed in terms of the dimensionless sphere radii r_l and r_s, the total area A of the multisphere leads to the area relation

$$N_l r_l^2 + N_s r_s^2 = 1\,. \tag{S27}$$

Note that this relation between r_l and r_s depends only on the sphere numbers N_l and N_s but does not involve any other parameter. Furthermore, the volume V of the same (N_l+N_s)-sphere leads to the volume relation

$$N_l r_l^3 \pm N_s r_s^3 = \bar{v} \tag{S28}$$

where the $\pm$ sign applies to positive and negative multispheres, respectively. The two relations as given by Eqs (S27) and (S28) explicitly show that the multisphere geometry depends only on the sphere numbers N_l and N_s as well as on the volume-to-area ratio $\bar{v}$.

S7 Positive two-sphere shapes with out-buds

S7.1 Stability regime for positive two-sphere shapes.

For positive spontaneous curvature, the two-sphere shapes in Fig 10a,b of the main text involve a positive ls-neck between the large and the small sphere. The condition for this ls-neck to be stably closed is given by the inequality[4]

$$m \geq M_{ls}^{\rm eff} = \tfrac{1}{2}\,(M_l + M_s) = \tfrac{1}{2}\left(\tfrac{1}{R_l} + \tfrac{1}{R_s}\right) > 0\,. \tag{S29}$$

In the limiting case, in which this inequality becomes an equality, we obtain the neck closure condition that determines the line of limit shapes $L_{1+1}^{\rm pos}$, see the upper boundary line of the stability regime in Fig 11 of the main text. The lower boundary line of the stability regime in this figure is provided by another line of limit shapes, which are provided by two equally sized spheres with radius $R_l = R_s = R_* = R_{\rm ve}/\sqrt{2}$ and are denoted by L_{2*}. In the morphology diagram, the latter line is located at $\bar{v} = 1/\sqrt{2}$ and $\bar{m} \geq \bar{m}_* = \sqrt{2}$.

The two lines of limit shapes, $L_{1+1}^{\rm pos}$ and $L_{2*}^{\rm pos}$, meet at the corner point with $\bar{v} = 1/\sqrt{2}$ and $\bar{m} = \bar{m}_* = \sqrt{2}$. The corresponding limit shape consists of two equally sized spheres with $M_l = M_s = M_* = m_*$, which implies that the bending energy $E_{\rm be}$ as given by Eq (S3)† vanishes for the two-sphere limit shape at the corner point.

As discussed in Sect 5.2 of the main text, the stability regime for positive two-spheres is divided up into several subregimes. The first subregime with positive mechanical tension, $\Sigma > 0$, is located between the line of limit shapes $L_{1+1}^{\rm pos}$ and the dashed red line in Fig 11 of the main text. The second subregime with negative mechanical tension, $\Sigma < 0$, is located between this dashed red line and the line of limit shapes L_{2*} with $\bar{m} > 2\sqrt{2}$. Furthermore, the small sphere transforms into a small prolate[4] for sufficiently large spontaneous curvatures with $\bar{m} > 13.29$, which is located to the right of the stability regime in Fig 11.

S7.2 Division of out-budded two-sphere vesicles

Within the stability regime for positive two-sphere shapes as displayed in Fig 12 of the main text, the vesicle shapes are stable against the opening of the closed neck. In addition, the closed neck is subject to a constriction force, which acts to compress the closed neck. For positive two-spheres, the constriction force $f^{\rm pos}$ has the form[4]

$$f^{\rm pos} = 8\pi\kappa\left(m - M_{\rm ne}^{\rm eff}\right) \quad \text{for } m \geq M_{\rm ne}^{\rm eff} \tag{S30}$$

with the effective mean curvature $M_{\rm ne}^{\rm eff} = M_{ls}^{\rm eff}$ for an ls-neck and $M_{\rm ne}^{\rm eff} = M_{**}^{\rm eff} = 1/R_*$ for two equally sized spheres with radius R_* along the $L_{2*}^{\rm pos}$-line. The force $f^{\rm pos}$ vanishes at the $L_{1+1}^{\rm pos}$-line with $m = M_{ls}^{\rm eff}$, including the corner point with $m = \sqrt{2}/R_{\rm ve}$, see Fig 12 of the main text, and attains a finite and positive value when the spontaneous curvature m exceeds the neck mean curvature $M_{\rm ne}^{\rm eff}$.

The constriction force $f^{\rm pos}$ as given by Eq (S30) increases when we increase the spontaneous curvature m. For sufficiently large values of m, the constriction force $f^{\rm pos}$ cleaves the closed membrane neck and divides the two-sphere vesicle into two daughter vesicles. Such a division process has been experimentally demonstrated

GUV label	B′	C′	D†	E†	F†
R_{ve} [μm]	2.7	4.2	6.16	4.60	4.10
$\bar{v}$	0.83	0.73	0.93	0.70	0.71
M_{ne}^{eff} [μm^{-1}]	0.204	0.340	0.441	0.308	0.345
X [nM]	7.8	7.8	31.2	39	15.6
mol% NTA	0.1	0.1	0.1	0.1	1
Γ [GFPs/μm^2]	53.8	53.8	216	269	1076
m [μm^{-1}]	1.45	1.45	5.81	7.26	29
$m - M_{ne}^{eff}$ [μm^{-1}]	1.246	1.11	5.37	6.95	28.7
f^{pos} [pN]	6.14	5.47	26.5	34.2	141
Σ [10^{-4}mN/m]	- 5.92	- 4.38	- 112	-189	- 3218

Table S1 Experimentally determined parameters for five two-sphere GUVs, denoted by B′, C′, D†, E†, and F† in Ref 6. The geometric parameters in the first three rows are the vesicle size R_{ve}, the volume-to-area ratio $\bar{v}$, and the positive effective mean curvature M_{ne}^{eff} of the closed neck connecting the two spheres. The next four rows are the nanomolar GFP concentration X in the exterior compartment and the mol% of NTA anchor lipids added to the membranes, which together determine the coverage Γ of the membrane by the GFP molecules as well as the spontaneous curvature m. The last two rows display the constriction force f^{pos} as given by Eq (S30), which is positive and increases from D† to F†, as well as the mechanical tension Σ, which becomes more and more negative from D† to F†, as follows from Eq (25) in the main text.

for GUVs by exposing the outer leaflet of the GUV membranes to His-tagged GFPs that bind to NTA anchor lipids within these membranes.[6] In the latter study, a two-step procedure was used to generate two-sphere shapes of vesicles. First, the GUVs were osmotically deflated to obtain prolate shapes; second, the spontaneous curvature was increased by increasing the GFP concentration in the exterior solution, until the vesicles formed two-sphere shapes as in Fig S15 .

The two-sphere vesicles B′ and C′ in Fig S15 represent two-sphere shapes that were stable on the exper-

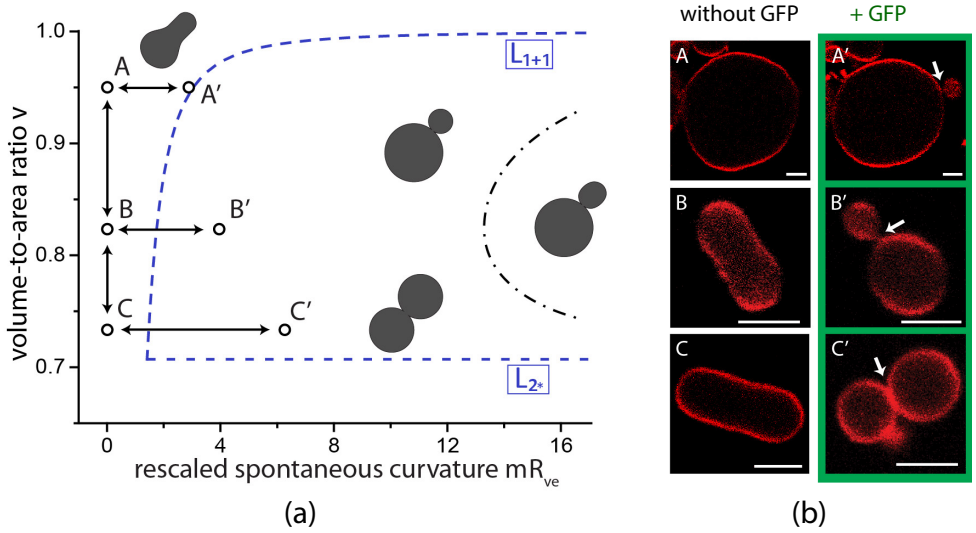

Figure S15 (a) Morphology diagram for giant vesicles as a function of rescaled spontaneous curvature $\bar{m}$ and volume-to-area ratio $\bar{v}$. Two-sphere vesicles with positive membrane necks are stable between the two dashed lines of limit shapes L_{1+1} and L_{2*} (blue). The latter subregion contains the dash-dotted line, at which the spherical out-bud becomes unstable and transforms into a prolate out-bud. The shapes denoted by A, B, and C correspond to three GUVs in the absence of GFP. Adding GFP to the exterior solution, the three GUVs transform into the dumbbell shapes A′, B′, and C′; and (b) Confocal images of the three vesicle shapes A′, B′, and C′ with closed membrane necks (white arrows).[6]

imentally accessible time scales. The corresponding geometric and curvature-elastic parameters are given in the first two columns of Table S1. The last three columns of this table provide the parameters of three GUVs, denoted by $D^{\dagger}$, $E^{\dagger}$, and $F^{\dagger}$ which were exposed to an increased GFP concentration X in the exterior solution, see 4th row of Table S1, which induced a strongly increased spontaneous curvature m, see 7th row of Table S1. As a consequence, the constriction force $f^{\rm pos}$ became sufficiently large, see 8th row in the table, to cleave the membrane neck and to divide the vesicle. Somewhat surprisingly, the GUVs were observed to undergo division for relatively low coverages Γ as follows from the 5th row of Table S1. Based on the values for the constriction force $f^{\rm pos}$ in the 8th row of Table S1 one may conclude that vesicle division requires a constriction force that exceeds a threshold value of about 25 pN.

Compared to Ref 6, Table S1 has been reordered and supplemented by the last row with the mechanical tension Σ within the GUV membranes. Inspection of this last row reveals that all GUV membranes experienced a negative mechanical tension. In addition, vesicle division was observed when the negative membrane tension exceeds the threshold value $\Sigma_{\rm th} \simeq -10^{-2}$ mN/m.

S8 Negative two-sphere shapes with in-buds

Stability regime of negative two-sphere shapes. For negative spontaneous curvature, the two-sphere shape consists of a large sphere that encloses a small inverted sphere, connected by a negative ls-neck, see Fig 10e in the main text. The stability condition for the negative ls-neck is given by the inequality[4]

$$m \leq M_{ls}^{\rm eff} = \tfrac{1}{2}\,(M_l + M_s) = \tfrac{1}{2}\left(\tfrac{1}{R_l} - \tfrac{1}{R_s}\right) < 0\,. \tag{S31}$$

In the limiting case, in which this inequality becomes an equality, we obtain the neck closure condition, $m = M_{ls}^{\rm eff}$, that determines the line of limit shapes $L_{1+1}^{\rm neg}$, see the upper boundary line of the stability regime in Fig S16 . The lower boundary line of the stability regime is provided by another line of limit shapes, denoted by $L_{2*}^{\rm neg}$, which consist of two equally sized spheres with radii $r_1 = r_2 = r_* = 1/\sqrt{2}$ and volume-to-area ratio $\bar{v} = 0$.

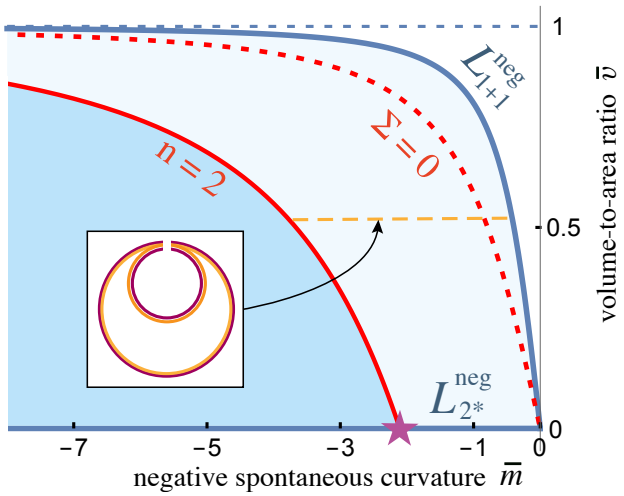

Figure S16 Stability regime (light blue) for negative (1+1)-spheres with negative spontaneous curvature $\bar{m}$. This stability regime is again bounded by two lines of limit shapes, $L_{1+1}^{\rm neg}$ and $L_{2*}^{\rm neg}$, which meet at the corner point $(\bar{m},\bar{v}) = (0,0)$. The persistent (1+1)-spheres along the red dashed line are characterized by tensionless membranes with mechanical tension $\Sigma = 0$; this tension is negative below the red dashed line and positive above this line. The inset displays a persistent (1+1)-shape that remains unchanged when we vary the spontaneous curvature along the horizontal dashed line (orange). This shape invariance is a direct consequence of the area and volume relations in Eqs (S27) and (S28). Along the red solid line, the spherical in-bud becomes unstable with respect to the spherical harmonics Y_{20} and transforms into a small prolate. The end point of the red solid line is located at $(\bar{m},\bar{v}) = (-3/\sqrt{2},0)$ (purple star).

Mechanical membrane tension of negative two-spheres. Along the line of limit shapes $L^{\rm neg}_{1+1}$ in Fig S16, the neck closure condition $M_l + M_s = 2M^{\rm eff}_{ls} = 2m$ as given by Eq (S31) implies the positive mechanical tension

$$\Sigma = 2\kappa m^2 = 2\kappa \left(M^{\rm eff}_{ls}\right)^2 \quad \text{for all limit shapes } L^{\rm neg}_{1+1} \tag{S32}$$

as follows from Eq (25) in the main text. One should note that the geometry of the limit shape $L^{\rm neg}_{1+1}$ changes with the spontaneous curvature m because the effective mean curvature $M^{\rm eff}_{ls} = m$ of the ls-neck becomes more negative with decreasing spontaneous curvature, $m < 0$. It also follows from Eq (25) in the main text that

$$\Sigma = 0 \quad \text{for} \quad m = M_l + M_s\,, \tag{S33}$$

which applies to the persistent shapes along the red dashed line in Fig S16. This red dashed line extends up to the corner point $(\bar{m}, \bar{v}) = (0,0)$ with two nested spheres of equal size and opposite mean curvature which implies $M_l + M_s = 0$.

Along the line of limit shapes $L^{\rm neg}_{2*}$ with $\bar{m} < 0$ and $\bar{v} = 0$, the negative $(1+1)$-sphere corresponds to two nested spheres of equal size and opposite mean curvature $M_l = 1/R_*$ and $M_s = -1/R_*$. As a consequence, the mechanical tension is given by

$$\Sigma = -2\kappa m^2 \quad \text{for the limit shapes } L^{\rm neg}_{2*}. \tag{S34}$$

For $\bar{m} < -3/\sqrt{2}$ (purple star in Fig S16), the inner sphere of the two nested spheres would like to transform into a prolate but this shape transformation is suppressed by the outer sphere enclosing the inner one.

The relationships for the mechanical tension Σ as given by Eqs (S32) – (S34) can be summarized as follows. The stability regime for negative two-spheres is divided up into several subregimes. The first subregime with positive mechanical tension, $\Sigma > 0$, is located between the line of limit shapes $L^{\rm neg}_{1+1}$ and the dashed red line in Fig S16. The second subregime with negative mechanical tension, $\Sigma < 0$, is located between the dashed red line and the line of limit shapes $L^{\rm neg}_{2*}$. The mechanical tension is equal to $\Sigma = +2\kappa m^2$ along the $L^{\rm neg}_{1+1}$-line and to $\Sigma = -2\kappa m^2$ along the $L^{\rm neg}_{2*}$-line. Furthermore, the mechanical tension Σ varies in a continuous manner across the corner point $(\bar{m}, \bar{v}) = (0,0)$, where $\Sigma = 0$.

Possible division of in-budded two-sphere vesicles. The closed membrane neck of a negative two-sphere vesicle is subject to the constriction force

$$f^{\rm neg} = 8\pi\kappa \left(M^{\rm eff}_{\rm ne} - m\right) \quad \text{for } m \le M^{\rm eff}_{\rm ne} < 0 \tag{S35}$$

with the effective mean curvature $M^{\rm eff}_{\rm ne} = M^{\rm eff}_{ls}$ for an ls-neck and $M^{\rm eff}_{\rm ne} = M^{\rm eff}_{**} = -1/R_*$ for two equally sized and nested spheres with radius R_* along the $L^{\rm neg}_{2*}$-line in Fig S16. The force $f^{\rm neg}$ vanishes along the $L^{\rm neg}_{1+1}$-line with $m = M^{\rm eff}_{ls}$, including the corner point with $m = 0$, see Fig S16, and attains a finite and positive value when the negative spontaneous curvature m is smaller than the negative effective mean curvature $M^{\rm eff}_{\rm ne}$.

The constriction force $f^{\rm neg}$ as given by Eq (S35) increases when we decrease the negative spontaneous curvature m towards more negative values. For sufficiently large and negative values of m, the constriction force $f^{\rm pos}$ will cleave the closed membrane neck and divide the negative two-sphere vesicle into two nested daughter vesicles. So far, such a division process has not been observed experimentally but should become accessible to GUV experiments when the inner rather than the outer leaflet of the GUV membranes is exposed to His-tagged GFPs that bind to NTA anchor lipids within these membranes. In this way, one will be able to generate a large negative spontaneous curvature that first leads to in-budded two-sphere vesicles and subsequently to neck cleavage and vesicle division. Alternatively, the division of negative two-spheres with in-buds should also be accessible to experiment when cationic peptides bind to anionic lipid headgroups within the inner leaflets of GUVs as recently proposed in Ref 27.

S9 Aqueous two-phase system of PEG and dextran

Phase diagram and interfacial tension. One aqueous two-phase system that has been studied in some detail is provided by aqueous solutions of PEG and dextran. The phase diagram of this system is displayed in Fig S17 a as a function of the weight fractions w_d and w_p of dextran and PEG. This phase diagram includes a broad two-phase coexistence region where the liquid mixture undergoes phase separation into a PEG-rich phase α and a dextran-rich phase β. The phase diagram exhibits a critical demixing point, which is located at room temperature on the binodal line with $w_\mathrm{d} = 0.0451$ and $w_\mathrm{p} = 0.0361$.

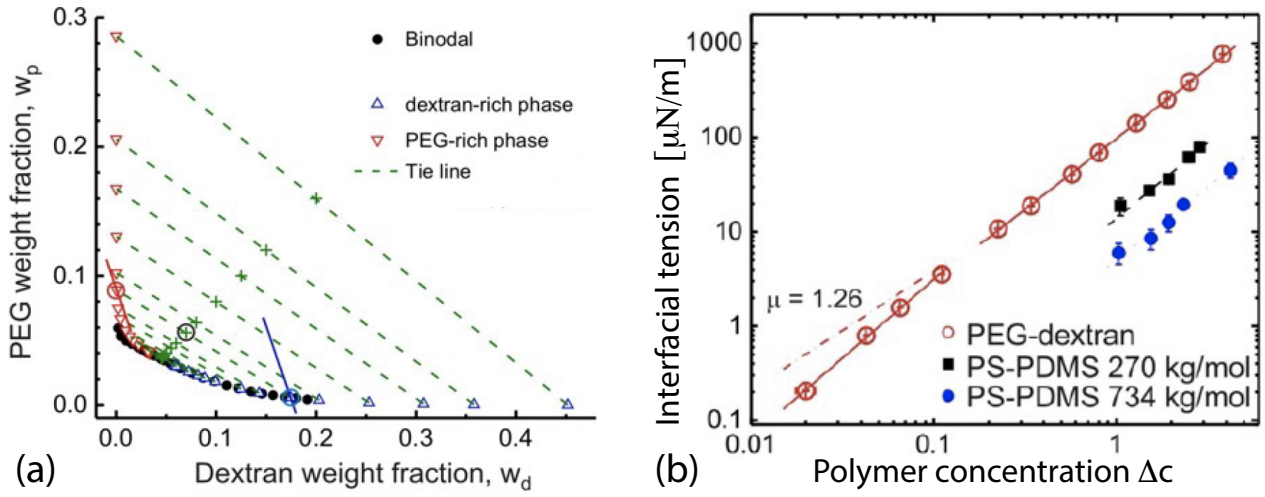

Figure S17 Aqueous two-phase systems formed by PEG and dextran: (a) Phase diagram at room temperature in terms of the weight fractions w_d and w_p of dextran and PEG. The binodal line (black and red data points) separates the one-phase region at low weight fractions from the two-phase region at higher weight fractions. The critical demixing point is at $w_\mathrm{d} = 0.0451$ and $w_\mathrm{p} = 0.0361$. The green dashed lines represent tie lines in the two-phase region. The solution phase separates into a PEG-rich phase α (red ∇-symbols) and a dextran-rich phase β (blue Δ-symbols); and (b) Interfacial tension $\Sigma_{\alpha\beta}$ of the liquid–liquid interface between the PEG-rich phase α and the dextran-rich phase β as a function of the polymer concentration $\Delta c \equiv (c - c_\mathrm{cr})/c_\mathrm{cr}$ where c_cr denotes the concentration at the critical demixing point. Reused with permission from ref. 28, American Chemical Society, 2012.

The interface between the condensate droplet and the surrouding liquid phase can be characterized by the interfacial tension $\Sigma_{\alpha\beta}$. For aqueous two-phase systems arising from PEG-dextran solutions, this interfacial tension has been measured over four orders of magnitude as shown in Fig S17 b. In this figure, the red data are well-fitted by the power-law behavior $\Sigma_{\alpha\beta} \sim \Delta c^{\mu}$ with the critical exponent μ close to the mean value[29] $\mu = 3/2$. For comparison, the dashed red line corresponds to $\mu = 1.26$ based on the hyper-scaling relation[30] $\mu = 2\nu$ where ν is the critical exponent of the correlation length. It is important to note that the interfacial tension $\Sigma_{\alpha\beta}$ provides a new tension scale for the vesicle-droplet systems.

Wetting of GUV membranes by PEG-dextran solutions. Phase separation of PEG-dextran solutions within GUVs can lead to partial or complete wetting of the GUV membranes as schematically shown in Fig S18 . Panel (a) of this figure displays the phase diagram of the liquid mixture as in Fig S17 a but with the coexistence region of this mixture being divided up into two subregions. Close to the critical point, the membranes are completely wetted by the PEG-rich α phase while they are partially wetted further away from this point. The corresponding wetting morphologies are depicted in Fig S18 b and c.

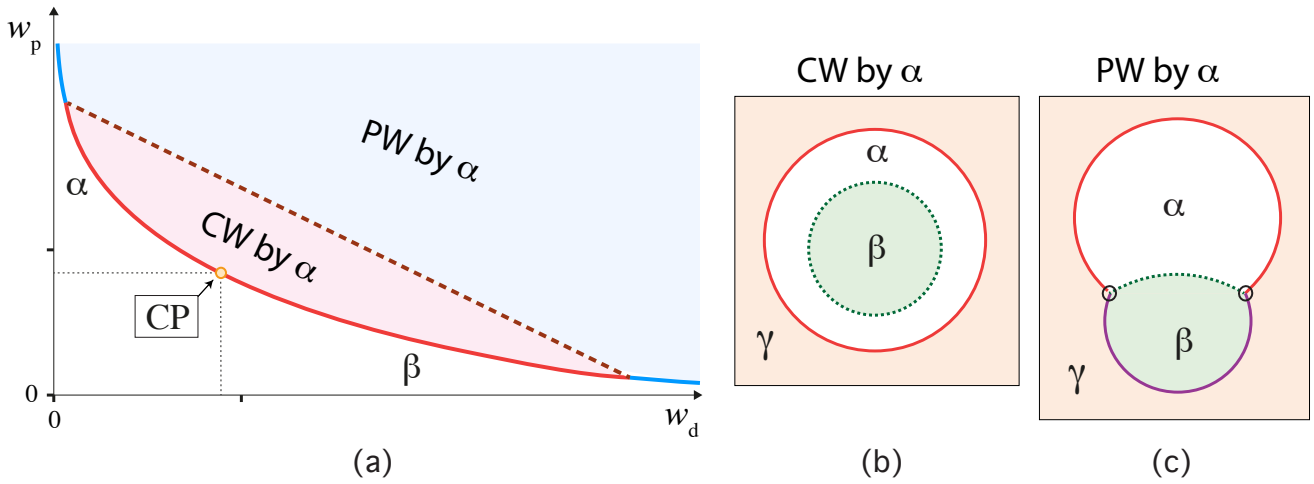

Figure S18 Wetting behavior of aqueous PEG-dextran solutions within giant vesicles, with the PEG-rich phase α and the dextran-rich phase β: (a) Schematic phase diagram of PEG-dextran solutions at room temperature. The phase diagram exhibits (i) a one-phase region (white) at low weight fractions w_d and w_p of the dextran and PEG polymers as well as (ii) a two-phase region (light red and light blue) at higher weight fractions. The boundary between the one-phase and two-phase regions defines the binodal line which contains the critical demixing point (CP, orange). The two-phase region above the binodal is divided up into two subregions, a complete wetting (CW) subregion (light red) close to the critical point and a partial wetting (PW) subregion (light blue), which are separated by a certain tie line (dashed purple line). The endpoints of this tie line divide the binodal line up into a red and two blue segments; (b) CW morphology and (c) PW morphology of the vesicle-droplet system corresponding to complete wetting of the vesicle membrane by the PEG-rich phase α and to partial wetting by both phases α and β.[31]

References

[1] W. Helfrich, *Z. Naturforsch.*, 1973, **28c**, 693–703.

[2] H. Deuling and W. Helfrich, *J. Physique*, 1976, **37**, 1335–1345.

[3] U. Seifert, K. Berndl and R. Lipowsky, *Phys. Rev. A*, 1991, **44**, 1182–1202.

[4] R. Lipowsky, *The Giant Vesicle Book*, Taylor & Francis, 2019, ch. 5, pp. 73–168.

[5] T. Bhatia, S. Christ, J. Steinkühler, R. Dimova and R. Lipowsky, *Soft Matter*, 2020, **16**, 1246–1258.

[6] J. Steinkühler, R. L. Knorr, Z. Zhao, T. Bhatia, S. Bartelt, S. Wegner, R. Dimova and R. Lipowsky, *Nature Commun.*, 2020, **11**, 905.

[7] M. do Carmo, *Differential geometry of curves and surfaces*, Prentice-Hall, Englewood Cliffs, NJ, USA, 1976.

[8] R. Lipowsky, *Adv. Colloid Interface Sci.*, 2014, **208**, 14–24.

[9] R. Osserman, *Bull. Am. Math. Soc.*, 1978, **84**, 1182–1238.

[10] S. Hildebrandt and A. Tromba, *Mathematics and Optimal Form*, American Scientific Library, New York, NY, USA, 1985.

[11] T. Bhatia, J. Agudo-Canalejo, R. Dimova and R. Lipowsky, *ACS Nano*, 2018, **12**, 4478–4485.

[12] R. Lipowsky and M. E. Fisher, *Phys. Rev. B*, 1987, **36**, 2126–2141.

[13] R. Lipowsky and S. Leibler, *Phys. Rev. Lett.*, 1986, **56**, 2541–2544.

[14] R. Lipowsky, *Fundamental Problems in Statistical Mechanics*, Elsevier Science Publishers, 1990, vol. VII, pp. 139–170.

[15] I. S. Gradshteyn and I. M. Ryzhik, *Table of Integrals, Series, and Products*, Academic Press, New York, 1980.

[16] P.-G. De Gennes and C. Taupin, *J. Phys. Chem.*, 1982, **86**, 2294–2304.

[17] G. Gompper and D. Kroll, *Phys. Rev. E*, 1995, **51**, 514–525.

[18] A. Mangiarotti, M. Aleksanyan, M. Siri, T.-W. Sun, R. Lipowsky and R. Dimova, *Adv. Sci.*, 2024, **11**, 2309864.

[19] R. Ghosh, V. Satarifard, A. Grafmüller and R. Lipowsky, *Nano Lett.*, 2019, **19**, 7703–7711.

[20] R. Lipowsky, R. Ghosh, V. Satarifard, A. Sreekumari, M. Zamaletdinov, B. Różycki, M. Miettinen and A. Grafmüller, *Biomolecules*, 2023, **13**, 926.

[21] M. Zamaletdinov, M. Miettinen and R. Lipowsky, *Soft Matter*, 2023, **19**, 6929–6944.

[22] A. Sreekumari and R. Lipowsky, *Soft Matter*, 2022, **18**, 6066–6078.

[23] M. Miettinen and R. Lipowsky, *Nano Lett.*, 2019, **19**, 5011–5016.

[24] A. Sreekumari and R. Lipowsky, *J. Chem. Phys.*, 2018, **149**, 084901.

[25] A. Grafmüller, J. C. Shillcock and R. Lipowsky, *Biophys. J.*, 2009, **96**, 2658–2675.

[26] R. Lipowsky, *Adv. Colloid Interface Sci.*, 2022, **301**, 102613.

[27] J. Steinkühler, R. Lipowsky and M. S. Miettinen, *J. Phys. Chem. B*, 2024, **128**, 8782–8787.

[28] Y. Liu, R. Lipowsky and R. Dimova, *Langmuir*, 2012, **28**, 3831–3839.

[29] J. W. Cahn and J. E. Hilliard, *J. Chem. Phys.*, 1958, **28**, 258–267.

[30] B. Widom, *J. Chem. Phys.*, 1965, **43**, 3892–3897.

[31] R. Lipowsky, *J. Phys. Chem. B*, 2018, **122**, 3572–3586.